J Fail. Anal. and Preven.
https://doi.org/10.1007/s11668-023-01833-2

ORIGINAL RESEARCH ARTICLE

Machine Learning Prediction of Aluminum Alloy Stress–Strain Curves at Variable Temperatures with Failure Analysis

Abdelhakim Dorbane · Fouzi Harrou · Daniel-Constantin Anghel · Ying Sun

Submitted: 17 October 2023 / in revised form: 19 November 2023 / Accepted: 21 November 2023

Abstract Accurately predicting stress–strain curves is essential for understanding the plastic behavior of metallic materials. This study investigates the effectiveness of machine learning (ML) methods in predicting stress–strain curves for aluminum alloys at different temperature levels. Specifically, three ML techniques, Gaussian process regression (GPR), neural network (NN), and boosted trees (BST), were utilized to predict the stress–strain response of Al6061-T6 at temperatures ranging from 25 to 300 °C. The performance of these ML models was evaluated using actual strain–stress measurements obtained from uniaxial tensile testing on Al6061-T6. A fivefold cross-validation approach was applied to train the models under investigation. Optimal parameters for the ML techniques were obtained during the training phase using the Bayesian optimization method to minimize mean absolute error. Four statistical metrics were employed to assess the accuracy of the predictions. The results of this study demonstrate the potential of machine learning methods in accurately predicting strain–stress measurements of materials. Additionally, the NN model outperformed the other models, achieving an average mean absolute error percentage of 0.213 and a coefficient of determination R^2 of 0.998. Furthermore, it was observed that crack initiation mechanisms varied with temperature; particle fracture dominated at temperatures up to 200 °C, while interfacial decohesion prevailed at 300 °C.

Keywords Machine learning · Artificial intelligence · Data-driven methods · Predictive modeling · Mechanical behavior · Aluminum alloys · Uniaxial tensile testing

Introduction

Introduced in 1935, Al6061-T6 is a precipitation-hardened aluminum alloy designed to meet the demand for a material with intermediate strength, exceptional toughness, and weldability under specific conditions [1, 2]. Its versatility has led to widespread utilization across various industries, including automotive, aviation, and watercraft. In the motocar sector, Al6061-T6 finds application in the manufacturing of diverse motocar panels, structural components, and wheels. Similarly, the aviation industry relies on this alloy for the production of critical structural elements like airfoils and fuselage. Furthermore, its remarkable resistance to corrosion, even in saltwater environments, has made it a preferred choice in the watercraft sector [3].

A. Dorbane (✉)
Smart Structures Laboratory (SSL), Engineering and Sustainable Development Laboratory (ESDL), Faculty of Science and Technology, University of Ain Temouchent, PO BOX 284, 46000 Ain Temouchent, Algeria
e-mail: abdelhakim.dorbane@univ-temouchent.edu.dz

F. Harrou · Y. Sun
Computer, Electrical and Mathematical Sciences and Engineering (CEMSE) Division, King Abdullah University of Science and Technology (KAUST), Thuwal 23955-6900, Saudi Arabia

F. Harrou
e-mail: fouzi.harrou@kaust.edu.sa

Y. Sun
e-mail: ying.sun@kaust.edu.sa

D.-C. Anghel
Piteşti University Centre, The National University of Science and Technology POLITEHNICA Bucharest, Bucureşti, Romania
e-mail: daniel.anghel@upit.ro

Published online: 14 December 2023

Numerous research studies have been conducted to investigate the microstructural and mechanical behavior of Al6061-T6 aluminum alloy. In a study by [4], the influence of heat treatment on the microstructural and mechanical properties of Al-6061 alloy with Scandium (Sc) was examined. The researchers found that the addition of Sc resulted in grain size refinement in the as-cast Al6061 alloy, leading to improved mechanical characteristics. Furthermore, solid solution and heat treatment were found to enhance the mechanical properties of Al6061 aluminum alloy. Another study conducted by [5] focused on evaluating the impact of heating on the microstructural features and mechanical properties of Al6061 alloy. The experimental investigation revealed that increasing the homogenization annealing temperature initially augmented the yield strength, tensile strength, and ductility of the alloy. However, beyond a certain point, these properties started to decrease. The study identified the optimal annealing temperature for this alloy as 575 °C. Several other research articles have been published investigating the microstructural and mechanical characteristics of Al6061 processed using various techniques, including extrusion [6], forging [7], rolling [8], equal channel angular pressing (ECAP) [9], and different joining processes [10–12]. These studies have contributed valuable insights into understanding the effects of different processing procedures on the microstructure and mechanical behavior of Al6061 alloy.

Despite its long history of use, the predictive modeling of the mechanical behavior of Al6061-T6 aluminum alloy remains an active area of research. Understanding and accurately forecasting the material's mechanical properties are essential for enhancing its performance and enabling efficient design practices. Recently, machine learning techniques have emerged as powerful tools for predictive modeling in various scientific and engineering fields such as the analysis of failure in welding techniques [13], manufacturing failures [14], cutting tool life prediction [15], cutting forces in hard turning process [16], and predicting and forecasting the mechanical behavior of welded metal alloys [17, 18].

Özkavak et al. [19] explored the use of machine learning methods to predict mechanical properties of AA 2024 aluminum alloy after aging at various temperatures and times. Their study employed artificial intelligence techniques, including CNN, ANN, and RFR, to predict hardness and bending strength from existing experimental data. The results indicated successful prediction of Al alloy properties. For Powder Metal (PM) 2024 Al alloy, the CNN algorithm produced the best results: RMSE 0.09068, *R*-Squared 0.93476, and MAE 0.06734. For Full Dense (FD) 2024 Al alloy, the CNN algorithm also excelled with RMSE 0.08578, *R*-Squared 0.94166, and MAE 0.06212. In another study, Hangai et al. [20] employed machine learning techniques to categorize the mechanical properties of aluminum foam, using X-ray computed tomography (CT) images. Their research successfully achieved a classification accuracy exceeding 95% in distinguishing aluminum foam samples with high and low compressive strengths. Furthermore, the authors pointed out the potential for enhancing accuracy further through the incorporation of additional training data. These findings suggest the possibility of establishing a non-destructive quality assurance method for aluminum foam products through the noninvasive acquisition of product images. In [21], Devi et al. addressed a common challenge faced by the manufacturing industry, specifically in achieving the desired properties of aluminum alloys. Traditional methods involve extensive experimentation and testing, leading to resource wastage and inconclusive outcomes. To mitigate this, the authors proposed an algorithm employing machine learning techniques such as linear regression (LR), artificial neural network (ANN), and k-nearest neighbor (KNN) to predict the mechanical properties of aluminum alloys. Notably, the KNN algorithm demonstrated superior predictive capabilities for tensile strength and hardness values, while ANN offers more precise results for yield strength. This approach significantly conserved time and energy resources in the prediction of mechanical properties for aluminum alloys. In [22], Cao et al. measured the mechanical properties and corrosion resistance of various heat-treated 7N01 aluminum alloys. They introduced a novel approach to establish the relationship between heat-treated processing parameters and these properties using machine learning methods. Generalized regression neural network (GRNN), support vector machine (SVM), and multiple linear regression (MLR) were employed for predicting mechanical properties, while GRNN and SVM, both common machine learning methods, were used for corrosion resistance prediction. Through the comparison of coefficient of determination (R^2) and mean absolute percentage error (MAPE), the study confirmed the effectiveness of GRNN and SVM for modeling and prediction. In [23], Ye et al. explored the importance of understanding the mechanical properties and hardness for the efficient application of friction stir welding (FSW) in the production of Cu and Al composites. Their study focused on the utilization of Relevance Vector Machine (RVM), Support Vector Machine (SVM), and Least Square Support Vector Machine (LSSVM) algorithms for hybrid modeling of mechanical properties and hardness in FSW. Subsequently, three modeling methods, namely hybrid LSSVM-RVM, hybrid SVM-RVM, and hybrid SVM-LSSVM, were applied to predict mechanical properties. The research evaluated the models using statistical indices, including R^2, RMSE, and RMSE/ymax. Notably, the R^2 values for tensile test and hardness area results were 0.9712

and 0.9126, respectively, indicating the efficiency of the hybrid LSSVM-RVM model in estimating mechanical and hardness properties. In [24], Xiong et al. developed a mechanical performance prediction model for aluminum alloy strips, making use of the Gray Wolf Optimization (GWO) algorithm and the Extreme Learning Machine (ELM) algorithm. The GWO–ELM model achieved an impressive correct rate of 100% for tensile strength, 97.5% for yield strength, and 77.5% for elongation when controlling the prediction deviation within ± 10%. The model's RMSE for tensile strength, yield strength, and elongation were 5.365, 11.881, and 1.268, respectively, showcasing its superior accuracy and stability in predicting these critical properties of aluminum alloy strips. The study highlighted the model's potential to significantly improve the production of aluminum alloy strips, offering a valuable alternative to traditional approaches. Moreover, Li et al. [25] explored the accelerated discovery of high-strength aluminum alloys using machine learning, with a focus on the Al-Zn-Mg-Cu alloy system (7xxx series). By leveraging machine learning-based composition and process optimization, they successfully identified an optimized alloy composition with exceptional mechanical properties, including a high ultimate tensile strength of 952 MPa and 6.3% elongation, all achieved through a cost-effective processing route. Notably, their investigation revealed the presence of the Al_8Cu_4Y phase in wrought 7xxx-T6 alloys, forming a nanoscale network structure along sub-grain boundaries, which is distinct from the common irregular-shaped particles. This study demonstrated the viability of using machine learning to expedite the discovery of 7xxx alloys with superior mechanical performance in the past. In the study by Altinkok [26], ANNs are employed to forecast the mechanical properties of α-Al_2O_3 particulate-reinforced Al–Si10Mg alloy composites produced through the stir casting process. The research explored the utility of ANNs in optimizing the production of these composites by predicting key mechanical properties. Soundararajan et al. [27] conducted research on A413 aluminum alloy processed through the squeeze casting route. They utilized an ANN model alongside statistical techniques to model and analyze the material's mechanical properties. This approach enables a deeper understanding of the relationship between process variables and the resulting mechanical properties, providing insights for improved production processes. In the study by Varol, Canakci, and Ozsahin [28], ANNs are used to model the effects of reinforcement properties on the physical and mechanical properties of Al2024-B4C composites manufactured through powder metallurgy. The research aimed to elucidate how variations in reinforcement properties impact the final composite's characteristics, facilitating more informed decisions in composite material design.

In the field of materials science and engineering, a fundamental challenge lies in accurately predicting stress–strain curves for various materials under diverse loading conditions. The development of a reliable and efficient predictive model is essential to streamline the evaluation of material behavior, reducing the dependence on time-consuming and expensive experimental testing, and thereby, helps in crucial for understanding their plastic behavior and formability. This study aims to explore the effectiveness of machine learning models in predicting the mechanical behavior of Al6061-T6 aluminum alloy. The motivation behind this investigation stems from the adaptability of machine learning-driven methods in modeling complex multivariate data. Three different machine learning methods were investigated in this study to forecast the strain–stress response of the 6061-T6 aluminum alloy at various temperature levels (25, 100, 200, and 300 °C): Gaussian process regression (GPR), boosted trees (BST), and neural network (NN). Real measurements were collected by conducting uniaxial tensile testing on the as-received material, which served as the basis for evaluating the performance of the investigated methodologies. The machine learning models were developed using training data and subsequently utilized to predict strain–stress curves. The results of the study highlighted the promising and superior prediction capabilities of the neural network approach compared to the boosted trees and Gaussian process regression methods in this specific application. Overall, this investigation demonstrates the potential of machine learning models in accurately predicting the mechanical behavior of the Al6061-T6 aluminum alloy. The findings contribute to enhancing our understanding of the alloy's response under different temperature conditions and emphasize the effectiveness of machine learning-driven approaches in modeling and predicting complex material behaviors.

The following sections in this research paper will explore the materials and methods employed, provide a description of the machine learning models used, present the results and their discussion, and offer general conclusions. These will encompass a summary of findings, an acknowledgment of limitations, and considerations for future research. This comprehensive approach aims to enhance comprehension of how machine learning has been applied to predict the mechanical properties of Al-6061-T6 material.

Materials and Methodologies

In our study, we investigated a marketable Al6061-T6 alloy with a thickness of 3 mm, which was obtained from McMaster Inc. This particular alloy is known for its age-

hardening properties. The designation "T6" signifies a specific aging process [29], wherein the material is subjected to a temperature of 160 °C for a duration of eighteen hours, followed by air cooling to ambient temperature.

The primary alloying elements in Al6061-T6 are silicon (Si) and magnesium (Mg) . However, the presence of iron (Fe) and manganese (Mn) can result in the formation of additional phases that do not initially exist. If manganese and chromium (Cr) are present, iron-rich phases such as "α-$(Fe, Mn)_3SiAl_{12}$ or α-$(Fe, Cr)_3SiAl_{12}$" can form. In the absence of manganese and chromium, the alloy may form β-$Fe_2Si_2Al_9$ or α-Fe_3SiAl_{12} phases, or a combination of both. Table 1 provides the nominal chemical composition of Al6061-T6, outlining the constituent elements and their respective proportions.

For the examination of the microstructure of the interrupted tensile tests, we adhered to standard metallographic sample preparation procedures. The process commenced by cutting the sample into 10 mm^2 square pieces, followed by embedding it in a phenolic hot working resin powder using a hydraulic-pneumatic automatic mounting press called "TechPress 2^{TM}." Subsequently, the mounted specimens underwent grinding, involving the use of 320, 600, and 1200 grit abrasive papers in sequential stages. Between each step, the specimens were rotated by 90°, and water served as a lubricant during this process. Polishing was then conducted with a 1 µm diamond polycrystalline suspension and later with a 0.04 µm colloidal suspension on Spec-Cloth. This step included the contra-rotation of the sample until achieving a clear, haze-free mirror surface, with the assistance of BlueLube as a lubricant. To prevent the polishing compound from embedding into the aluminum matrix, we exercised caution to avoid applying excessive force during the grinding and polishing stages.

Tensile Testing

For conducting the tensile tests, an MTS Insight electromechanical testing instrument with a 30 KN load cell, computer control, and an "LBO-series Thermocraft LabTemp" furnace was utilized. The tensile test specimens were fabricated using CNC machining, and their geometric configuration is depicted in Fig. 1. To ensure consistency, the specimens were oriented such that their primary axes were parallel to the plate rolling direction, following the guidelines of ASTM E2448-11 [31]. The rolling direction, transverse direction and normal direction are referred as RD, TD and ND, respectively (Fig. 2).

Tensile tests were conducted to investigate the mechanical behavior of Al6061-T6 over a range of temperatures from ambient temperature (25 °C) to 300 °C, employing a strain rate of 10^{-3} s^{-1}. Prior to initiating each test, the specimens were subjected to a 30-min period within the furnace to attain a homogenized temperature. To preserve the microstructural morphology, the samples were promptly water-cooled after the completion of each test. To ensure the reproducibility of the results, each loading scenario was repeated at least twice.

Prediction Models

In this section, we provide a concise overview of the fundamental principles behind the models under consideration, namely GPR, Boosted Trees, and Neural Networks. Subsequently, we introduce the effectiveness metrics utilized to assess the performance of these investigated models.

GPR Model

Gaussian Process Regression (GPR) is a powerful kernel-based learning algorithm utilized in modeling multivariate data [32, 33]. It is particularly effective in revealing intricate relationships between multiple process variables based on training data, making it a valuable tool for tackling complex nonlinear regression problems. One of GPR's standout features is its distribution-free learning, enabling it to handle diverse data types that do not strictly adhere to Gaussian distributions [34]. The GPR-based prediction approach has demonstrated favorable performance in diverse domains, including swarm motion prediction [35], wind power prediction [36], and COVID-19 spread forecasting [37]. These applications highlight the efficacy of GPR in accurately predicting outcomes and its versatility in accommodating various types of data and uncertainties. In GPR, a nonparametric Bayesian approach, the response $\boldsymbol{y}$ of a function f at the input $\boldsymbol{x}$ is expressed as:

$$y_i = f(x_i) + \varepsilon_i \quad \text{(Eq 1)}$$

Where $\varepsilon \sim \mathcal{N}(0, \sigma_\varepsilon^2)$. This equation resembles the hypothesis in ordinary linear regression, where the output

Table 1 Nominal chemical composition of Al6061 alloy [30]

Wt.%	Al	Mg	Si	Cu	Cr	Fe	Zn	Mn	Ti	Other each	Other, total
Min	95.8	0.8	0.4	0.15	0.04	…	…	…	…	…	…
Max	98.6	1.2	0.8	0.4	0.35	0.7	0.25	0.15	0.15	0.05	0.15

consists of independent inputs x contaminated with additive noise ε.

GPR is characterized by flexibility and its ability to provide uncertainty estimates by assuming a Gaussian Process (GP) prior for the regression functions f(x) [38, 39]. Given input–output data $D = \{(x_i, y_i)\}_{i=1}^{n}$ and the assumption that $f(.)$ follows a Gaussian process, the GP prior distribution is expressed as:

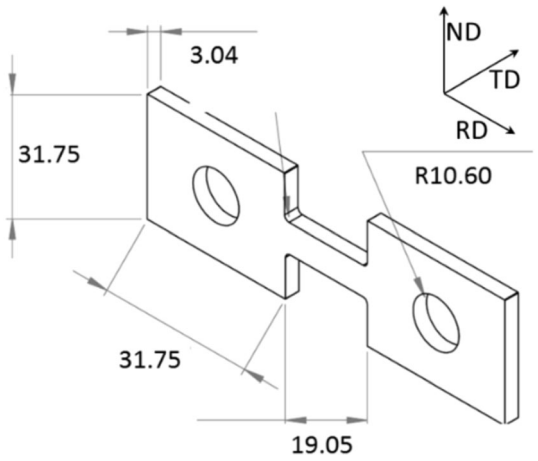

Fig. 1 Tensile testing samples geometry

$$f(x) \sim GP(m(x), k(x, x')) \quad \text{(Eq 2)}$$

The GP is entirely defined by its mean function, denoted as $m(x)$, and its kernel or covariance function, represented as $k(x, x')$.

$$m(x) = \mathbb{E}[f(x)] \quad \text{(Eq 3)}$$

$$k(x, x') = E[(f(x) - m(x))(f(x') - m(x'))] \quad \text{(Eq 4)}$$

These equations highlight that the mean and kernel functions can be adjusted to tailor the regression process to model the evolution of the specific physical process under consideration. The kernel function, in particular, plays a crucial role in describing the data structure and capturing the correlations between data points in a dataset. Various kernels are employed in GPR, and the most commonly used ones include the Radial Basis Function (RBF) kernel, the Matérn kernel, and the Polynomial kernel. Additional information regarding the GPR model can be referenced in [40, 41].

Several machine learning methods, including GPR and ensemble models, involve various hyperparameters, such as kernel types in GPR, which significantly affect model performance [40]. To determine the best hyperparameter values, common optimization techniques like grid search,

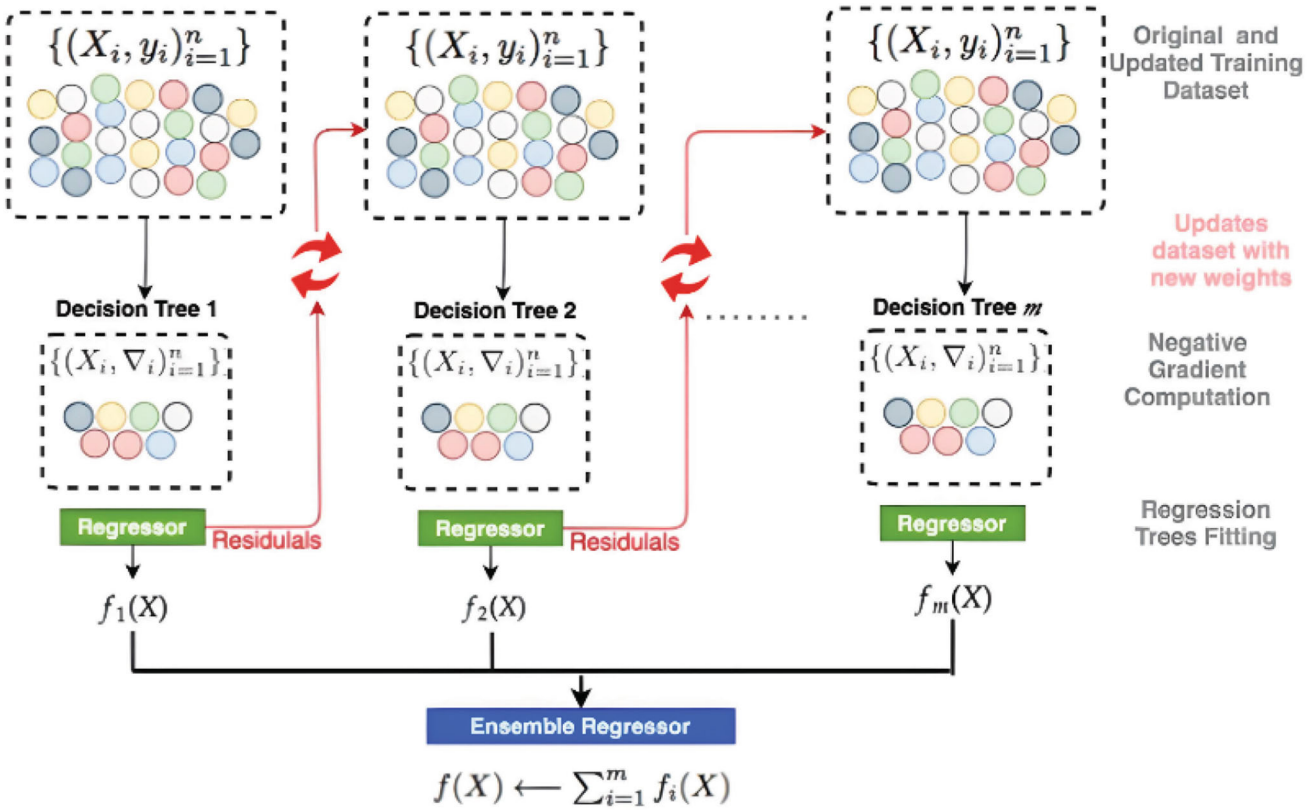

Fig. 2 A schematic representation depicting the concept of the Boosted Tree Regression approach

random search, and Bayesian Optimization (BO) are employed [41]. Grid search evaluates hyperparameter settings at predefined points within the search space, while random search explores hyperparameter combinations randomly, albeit without a guarantee of the best outcome. In this study, Bayesian Optimization, an efficient global optimization method based on Gaussian processes and Bayesian inference, was used. Bayesian Optimization reduces the time needed to find optimal parameters by considering past evaluations when selecting the next set of hyperparameters to evaluate. Unlike grid search, BO can achieve optimal hyperparameters with fewer iterations [42]. BO will be utilized to optimize hyperparameters for the following methods: GPR, Boosted Trees, and Neural Networks.

Boosted Tree Technique

Now, we discuss another important data-driven model called Boosted tree (BST), which is developed based on the statistical learning theory. The key concept of this approach is related to its ability to optimize the prediction accuracy of conventional regression techniques via an adaptive combination of weak predictors [43]. The basic idea of the Boosted Trees algorithm is to combine multiple decision trees to create a strong predictive model [43, 44]. It does this by sequentially training decision trees on the errors made by the previous ones (Fig. 3). Each new tree focuses on the residuals of the ensemble, which allows the model to improve its accuracy over time. The final prediction is a weighted sum of the predictions from all the trees, with more weight given to the trees that perform better. This iterative process of boosting enhances the model's ability to handle complex relationships in the data and is widely used in both classification and regression tasks. Using an aggregate model, smaller errors can be achieved by the BST compared to those acquired by single models [35]. When compared to other ensemble techniques like stacking, bagging, and model averaging, boosting stands out for its unique characteristic of sequentiality [43, 45].

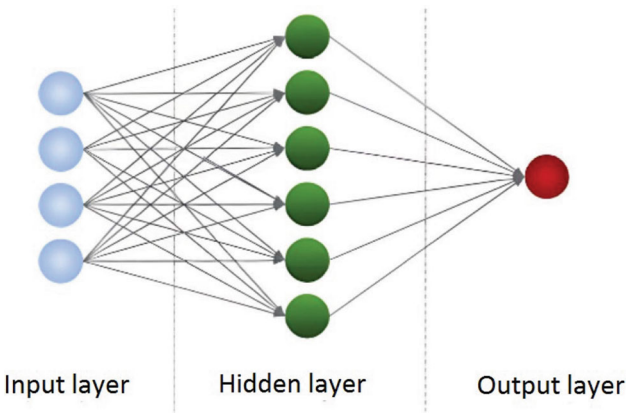

Fig. 3 Schematic presentation of ANN Structure

Neural Network

In the context of regression, neural networks serve as powerful tools for approximating and modeling complex relationships between input variables and continuous output values [46]. This approach offers a versatile and data-driven solution for tasks like predicting prices, estimating values, or forecasting outcomes. Neural networks, with their ability to learn intricate patterns and nonlinear associations within data, can significantly enhance our capacity to make accurate numerical predictions. Within this study, we harnessed a trilayered neural network enhanced by three hidden layers to execute predictive tasks [47]. This architecture affords the capacity to capture more intricate relationships between input and output variables compared to simpler designs, such as single-layer perceptrons or multilayer perceptrons featuring fewer hidden layers. Nonetheless, the adoption of a more intricate model heightens the potential for overfitting, underscoring the significance of employing regularization techniques like dropout or weight decay. A trilayered neural network, also known as a three-layer neural network or a feedforward neural network with a single hidden layer, is a fundamental architecture in artificial neural networks and machine learning. It consists of three primary layers, as shown in Fig. 3.

Input Layer: The input layer is the first layer of the neural network and is responsible for receiving the raw input data or features. Each neuron in this layer represents a specific feature or input variable, and these neurons pass the input values to the subsequent layer.

Hidden Layer: The hidden layer is an intermediate layer between the input and output layers. It plays a crucial role in learning and extracting complex patterns and representations from the input data. The number of neurons in the hidden layer is a user-defined hyperparameter, and it affects the network's ability to capture complex relationships within the data. The activation functions applied to the neurons in this layer introduce nonlinearity, which allows the network to model nonlinear relationships in the data.

Output Layer: The output layer is the final layer of the neural network and produces the network's predictions or outputs. The number of neurons in this layer depends on the nature of the task; for instance, in a binary classification problem, there might be one neuron for each class, while in a regression problem, there may be just one neuron for a single numeric prediction. The output layer typically

employs an activation function suited to the task, such as a sigmoid function for binary classification or a linear function for regression.

The input nodes in the input layer transfer the data to the hidden layer nodes using interconnected links. The inputs are multiplied with weights and passed to the next nodes. In Eq 5, H represents the size of the hidden layer, $\{V_{ih}$, i = 0,1,2,..,p, h = 1,2,.,H$\}$ denotes the synaptic weights connecting the hidden layer to the p-sized input, and $\{w_h$, h = 0,1,2,.,H$\}$ represents the synaptic weights connecting the output layer to the hidden layer. The outcome of the ANN, given an input vector (x_(1),...,x_p), is represented by Eq 5.

$$O = W_o + \sum_{h=1}^{H} w_h g\left(v_{oh} + \sum_{i=1}^{P} v_{th} x_i\right) \quad \text{(Eq 5)}$$

Prediction Framework

In this study, a general approach was employed to predict the strain–stress curve (Fig. 4). The data were initially divided into two parts: a training set (70%) and a testing set (30%). The prediction models were constructed using the training set, and a fivefold cross-validation strategy was adopted during the training process to mitigate the risk of overfitting. This approach ensured that the models were trained on a diverse range of data and enabled the evaluation of their performance on unseen test data. The forecasting framework encompasses two primary stages: model construction and model forecasting. Initially, data preprocessing is conducted, involving the removal of outliers and the handling of missing values. While the dataset employed in this study is devoid of any missing values, it is worth noting that missing data can arise during the collection of experimental samples due to various factors, such as sensor malfunctions or degradation. The literature offers a range of methodologies for imputing missing data [48]. The model is trained using the training data and then applied to predict the future trends in the strain–stress curve during the testing phase.

To assess the accuracy of the predictions in this study, four statistical metrics were utilized: coefficient of determination (R^2), mean absolute percentage error (MAPE), mean absolute error (MAE), and root mean square error (RMSE). These metrics provide a comprehensive evaluation of the prediction quality, taking into account both the magnitude and direction of the errors. By employing these metrics, a comprehensive assessment of the predictive performance can be obtained, aiding in the determination of the reliability and effectiveness of the models.

$$R^2 = \frac{\sum_{t=1}^{n} [(y_t - \overline{y}) \cdot (\hat{y}_t - \overline{y})]^2}{\sum_{t=1}^{n} (y_t - \overline{y})^2 \cdot \sum_{t=1}^{n} (\hat{y}_t - \overline{y})^2} \quad \text{(Eq 6)}$$

$$\text{RMSE} = \sqrt{\frac{1}{n} \sum_{t=1}^{n} (y_t - \hat{y}_t)^2} \quad \text{(Eq 7)}$$

$$\text{MAE} = \frac{\sum_{t=1}^{n} |y_t - \overline{y}_t|}{n} \quad \text{(Eq 8)}$$

$$\text{MAPE} = \frac{100}{n} \sum_{t=1}^{n} \left| \frac{y_t - \hat{y}_t}{y_t} \right| \% \quad \text{(Eq 9)}$$

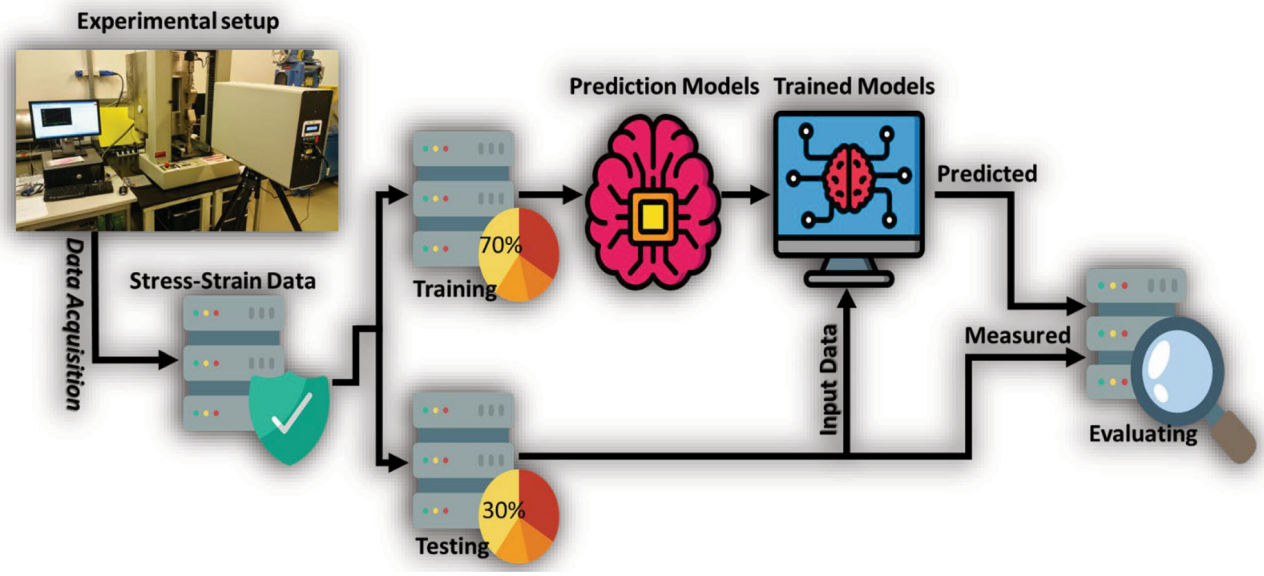

Fig. 4 Schematic drawing of the adopted prediction framework

where y_t is the actual stress, $\widehat{y_t}$ as its prediction, and n as the number of samples. A good quality of prediction is indicated by lower values of RMSE, MAE, and MAPE and R_2 value near 1. These metrics serve as measures of accuracy and precision, with lower values representing a closer agreement between the predicted and actual values. By achieving lower RMSE, MAE, and MAPE values and R_2 values near 1, the predictive models demonstrate a higher level of performance and reliability in capturing the true characteristics of the data.

Results and Discussion

Fractography Observations

Scanning electron microscopy (SEM) was utilized to examine the fracture surfaces of specimens subjected to tensile testing at ambient temperature (25 °C), 100, 200 and 300 °C under a strain rate of 10^{-3} s^{-1}. Figure 5 displays the SEM fractographs, revealing the presence of small dimples and coalesced micro-voids, indicative of a ductile fracture mechanism in Al6061-T6 [49]. Interestingly, Fig. 5a illustrates the occurrence of iron-rich phases at the bottom of certain micro-voids, highlighted by white circles [50]. These microscopic dimples exhibit variations in size and depth, with the average dimensions found to be smaller at 300 °C compared to 25, 100 and 200 °C. It should be noted that the depth of these dimples can be roughly correlated with the ductility of the metallic alloy [51]. Specifically, specimens tested at 25, 100 and 200 °C demonstrate greater strain to failure, accompanied by relatively deeper microscopic dimples (Fig. 5a-c). Conversely, specimens tested at 300 °C exhibit reduced strain to failure and display shallower microscopic dimples. A previous study by [52] demonstrated that at temperatures between 25 and 200 °C under a strain rate of 10^{-3} s^{-1}, crack initiation is attributed to second phase particles, whereas at 300 °C, crack initiation primarily occurs through interfacial decohesion (Fig. 5d). This finding explains the absence of second phase particles at the bottom of the microscopic dimples at 300 °C.

To go deeply into the investigation of the damage mechanisms that occurs at various temperatures for our material under investigation, interrupted tests were performed. The examination of the microstructure of interrupted tensile tested specimens serves as a critical step in understanding the behavior and performance of

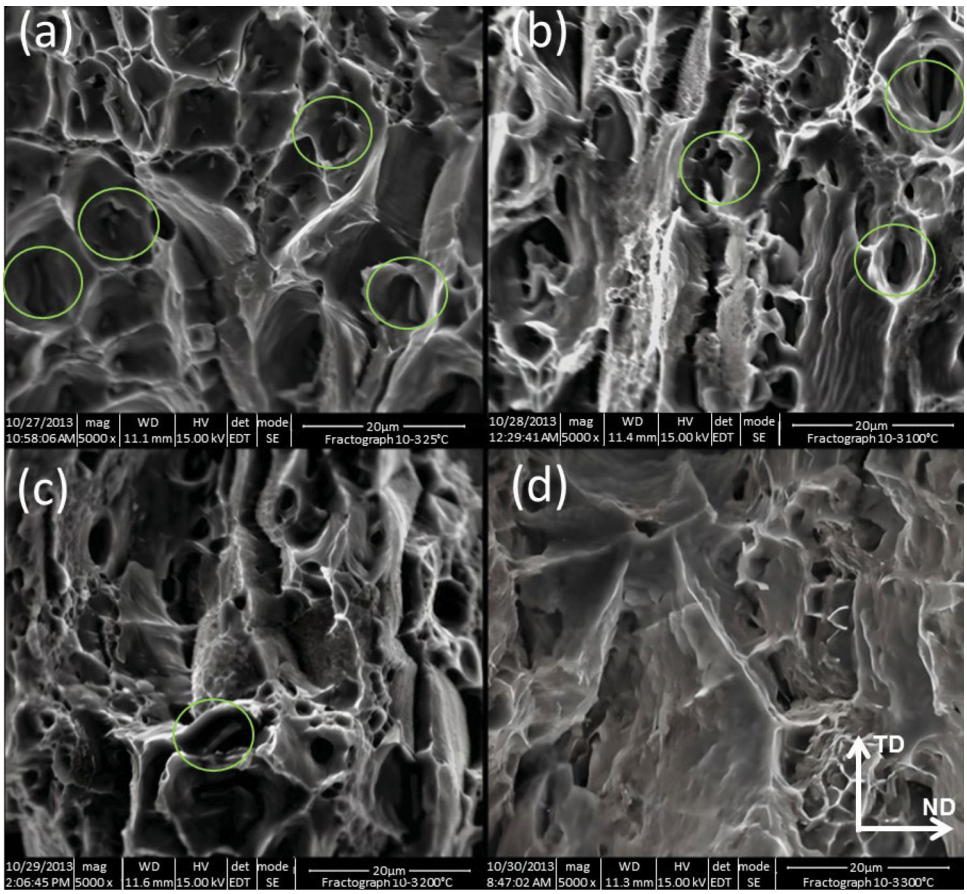

Fig. 5 SEM fractographs observations of tensile tested samples, (**a**) at ambient temperature (25 °C), and (**b**) at 100 °C, (**c**) at 200 °C and (**d**) at 300 °C

materials under mechanical stress. This examination aids in identifying microstructural features such as dislocations, grain boundaries, and defects, which play a pivotal role in a material's strength and ductility. It provides essential information on the mechanisms of material deformation and fracture, helping to elucidate the root causes of failure and the potential for material improvement. Moreover, studying the microstructure after interrupted tensile testing enables the assessment of the effect of variables like temperature and loading rate on material behavior. To discern the specific damage mechanisms governing the fracture characteristics of Al6061-T6, we tracked the initiation and progression of cracks in specimens subjected to loads at both 200 and 300 °C. As reported previously by Thomson and Hancock, [53], the plastic deformation of ductile metals and their alloys is constrained by the rates of void nucleation, growth, and their subsequent coalescence.

Figure 6 exhibits SEM micrographs of a specimen extracted from an interrupted test conducted at the inception of strain leading to failure. Figure 6a and b shows SEM micrographs of samples tested at a strain rate of 10^{-3} s^{-1} and a temperature of 200 °C. Notably, the micrographs reveal the presence of cracks, predominantly situated between fractured second-phase particles or visibly iron-rich phases represented by white particles. These microvoids were discernible in both the RD-ND and RD-TD planes but predominantly in the RD-ND plane. A similar phenomenon was previously documented by [50] in tests conducted at room temperature. It is essential to recognize that the iron-rich phase particles act as stress concentration sites that precipitate crack initiation, as evidenced by the void growth parallel to the loading direction, aligning with previous research [54]. These observations offer insights into the presence of iron-rich phases at the base of the observed microvoids on the fractograph surfaces in Fig. 5.

Conversely, in Fig. 6c and d, SEM micrographs display samples tested at a strain rate of 10^{-3} s^{-1} and a temperature of 300 °C. These micrographs distinctly illustrate the fracture progression in the necked region, characterized by parallel crack propagation that ultimately converges within localized shear bands formed in the thinned ligament between adjacent voids, as evident in Fig. 6c. Notably, Fig. 6d highlights the transverse direction (TD) as the path of crack propagation. In contrast, within the RD-ND plane, numerous cracks are distributed throughout the micrograph, with slight propagation along the rolling direction (RD) and subsequent coalescence within localized shear bands, as demonstrated in Fig. 6c. This pattern of crack propagation

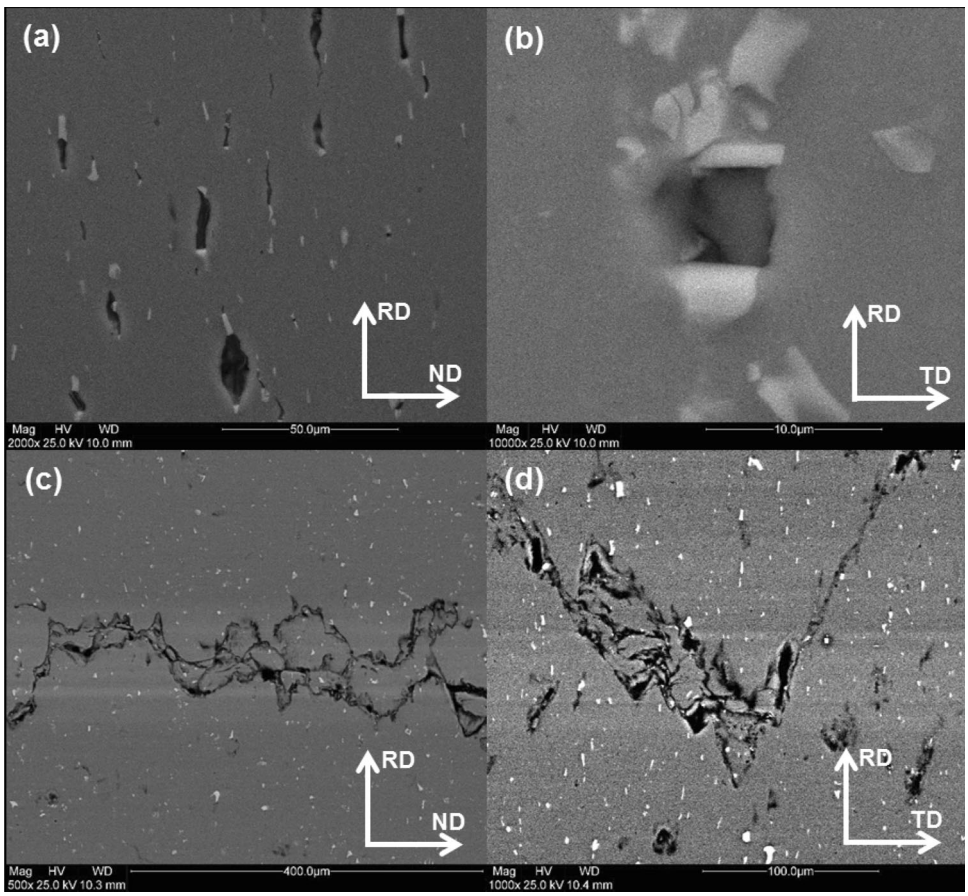

Fig. 6 SEM Analysis of Al6061-T6 Uniaxial Tensile Tests at 10^{-3} s^{-1} and: 200 °C: in (**a**) RD-ND and (**b**) RD-TD Planes, and at 300 °C: in (**c**) TD-RD and (d) ND-RD Planes

parallel to the transverse direction (TD) and the coalescence of cracks in the RD-ND plane results in the emergence of a macroscopic crack advancing at an angle relative to the normal direction (ND) within the RD-ND plane, ultimately culminating in the catastrophic failure of the sample. It is worth noting that the intermetallic phase particles remain unfractured, and the cracks tend to develop around these particles. At 300 °C, crack initiation is primarily attributed to interfacial decohesion, in contrast to the mechanisms observed at 200 °C and room temperature (RT).

Forecasting Results

Stress–Strain Data

In this investigation, the behavior of the Al6061-T6 alloy was examined by conducting uniaxial tensile testing at various temperatures, namely 25, 100, 200 and 300 °C under a constant deformation rate of 10^{-3} s^{-1}. Figure 7a presents the stress–strain data curves of the above-mentioned conditions; from this figure, it can be observed that the ultimate tensile strength is decreasing with increasing temperature, indicating the presence of a temperature sensitivity effect [52]. Also, Fig. 7a shows the presence of work hardening and work softening for the tensile tests ranging from ambient temperature to 200 °C; however, at 300 °C, there is only work softening effect, which might be due to creep phenomena [29].

To further understand the results provided by the tensile tests data, stress data distribution boxplot is established in Fig. 7b, and a stress data distribution boxplot is a graphical representation that offers valuable insights into the statistical distribution of stress values within a dataset. It serves as a concise summary of key characteristics of the stress

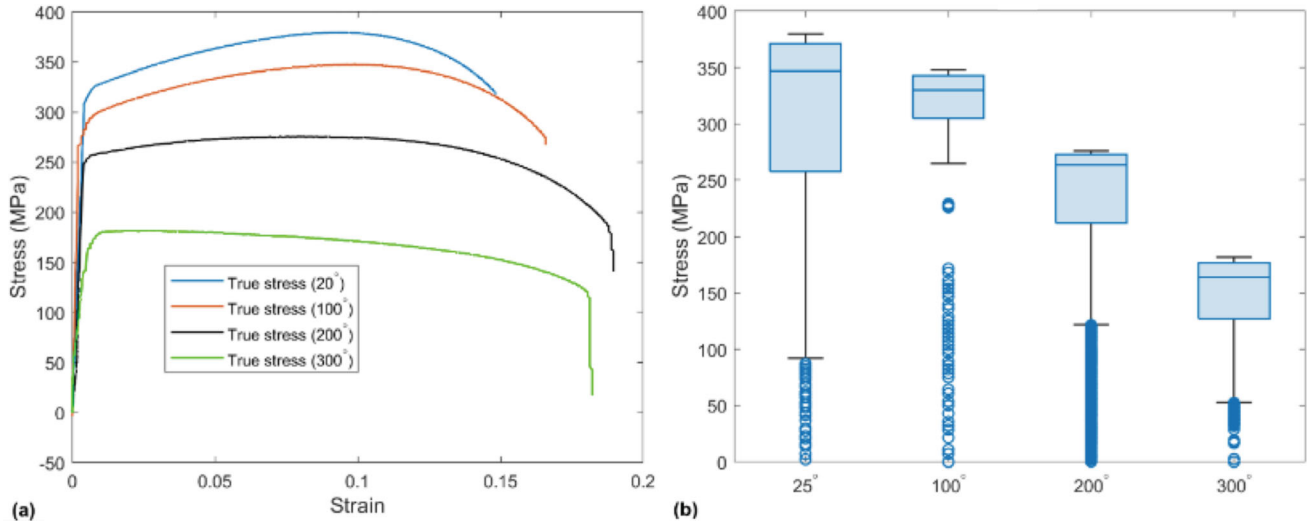

Fig. 7 (**a**) Strain–stress curves at different temperature levels, and (**b**) Stress data distribution of the as-received material

Table 2 Range of hyperparameter search and optimized hyperparameters using the Bayesian optimization algorithm

Model	Hyperparameter Search Range	Optimized Hyperparameters
GPR	Sigma: 0.0001–899	Sigma: 0.13811
	Basis function: Linear	Basis function: Linear
	Kernel function: Squared Exponential	Kernel function: Squared Exponential
BST	Number of learners: 10–500	Number of learners: 47
	Minimum leaf size: 1–795	Minimum leaf size: 1
	Number of predictors to sample: 1–2	Number of predictors to sample: 2
	Learning rate:0.1	Learning rate:0.1
TNN	Activation: ReLU, Tanh, Sigmoid,	Activation: Tanh
	Regularization Strength: 6.28e−09–62.89	Regularization Strength: 0.00156
	First Layer size: 1–300	First Layer size: 1
	Second Layer size: 1–300	Second Layer size: 11
	Third Layer size: 1–300	Third Layer size: 2

data, including its central tendency, variability, potential outliers, and skewness. The central tendency is represented by the median, located at the center of the box, while the size of the box (interquartile range) indicates the data's spread. Outliers, which significantly deviate from the bulk of the data, are often displayed outside the whiskers of the boxplot. Additionally, the orientation of the boxplot can reveal whether the data are skewed in one direction. Boxplots are excellent for comparing stress distributions between different groups or conditions, making them a powerful tool for quickly grasping the main features of the data and identifying areas of interest or concern within the stress dataset.

Stress–Strain Modeling

The dataset was initially split into two segments: a training set, which constituted 70% of the data, and a testing set, encompassing the remaining 30%. For the development of the prediction models, the training set was utilized. A fivefold cross-validation approach was applied to train the models under investigation. Optimal parameters for Gaussian process regression (GPR), boosted trees (BST), and the trilayered NN techniques were obtained during the training phase, using the Bayesian optimization method to minimize mean absolute error. The computed hyperparameter values for the considered models through Bayesian optimization are presented in Table 2.

Figure 8a-d presents the strain–stress values of the base material; both actual and predicted, using the BST, neural network (NN), and GPR models trained with the training data at temperatures of 25, 100, 200, and 300 °C. The results depicted in Fig. 8 demonstrate the effective predictive capability of all three models when trained with the provided dataset.

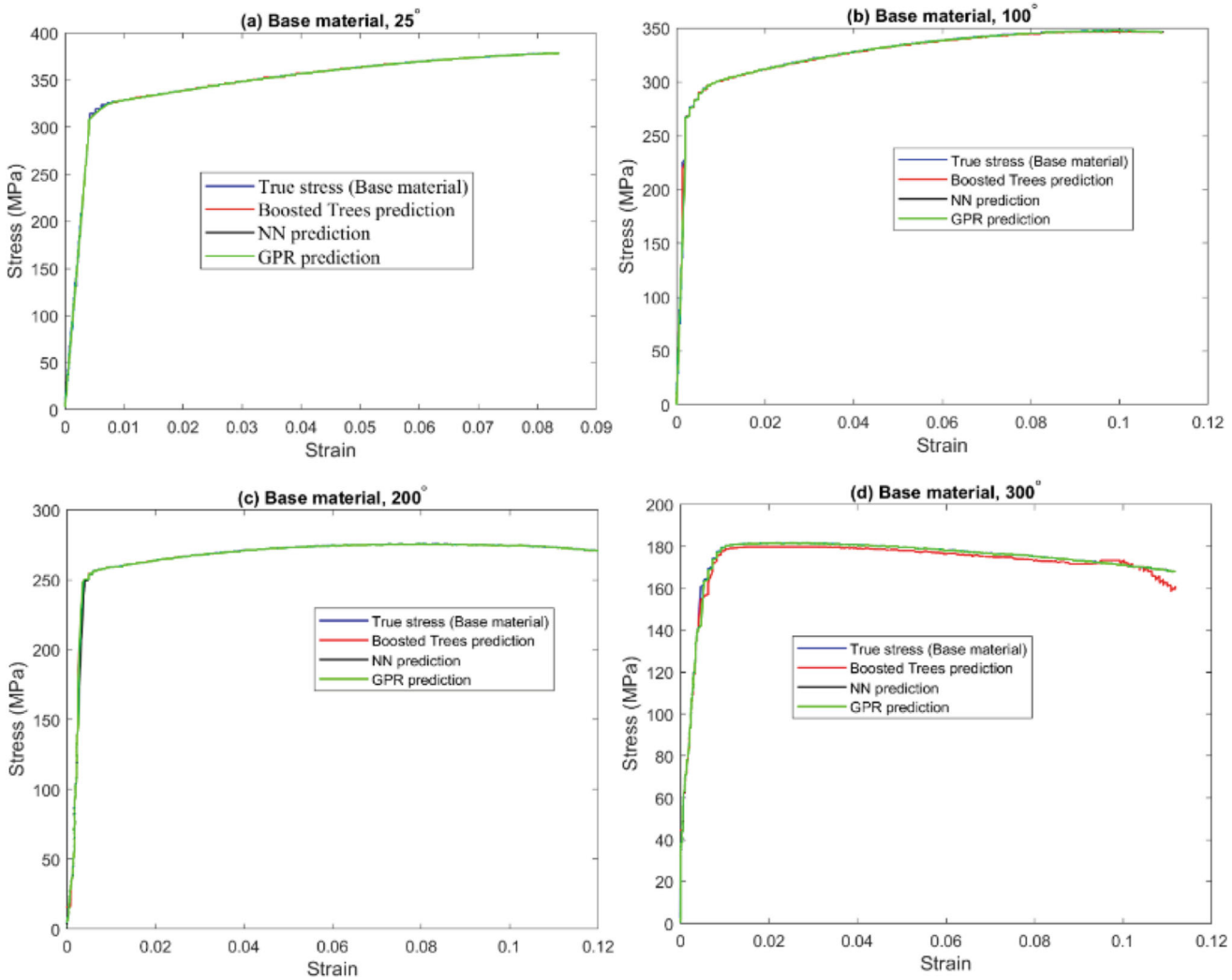

Fig. 8 Prediction results of stress–strain curves of base material utilizing the three methods: at (**a**) 25 °C, (**b**) 100 °C, (**c**) 200 °C and (**d**) 300 °C

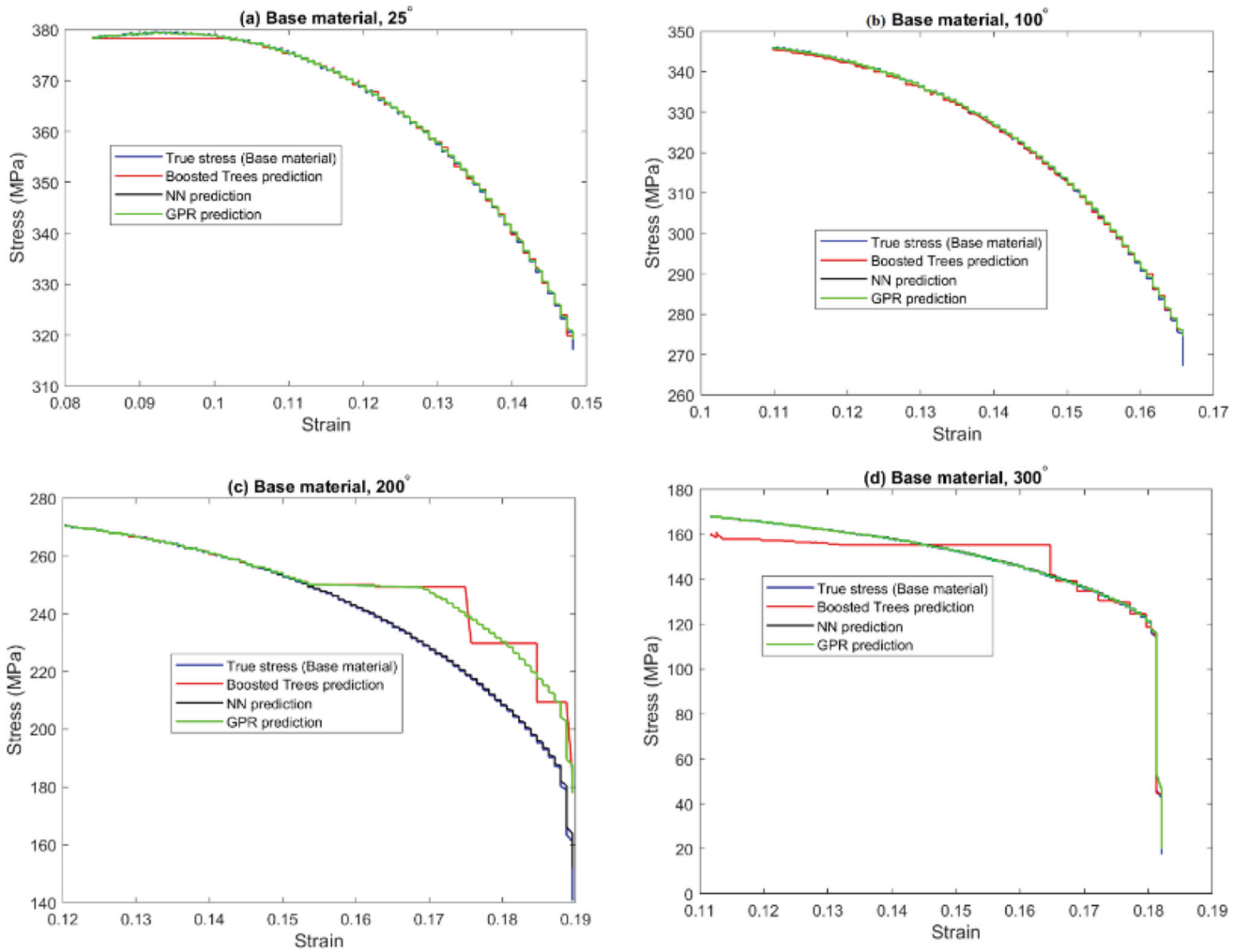

Fig. 9 Prediction results of stress–strain curves of the base material utilizing three models based on testing data under (**a**) 25 °C, (**b**) 100 °C, (**c**) 200 °C, and (**d**) 300 °C

Stress–Strain Forecasting

The prediction performance of the trained models using new testing data was evaluated in this section. Figure 9a-b displays the actual stress–strain curves along with the corresponding predictions obtained from the boosted trees (BST), neural network (NN), and Gaussian process regression (GPR) models for the material under investigation. It can be observed that both the BST and NN models exhibit satisfactory prediction performance. However, it is evident that the GPR model does not provide acceptable prediction accuracy.

Table 3 provides a comprehensive overview of the evaluation metrics for predicting the mechanical behavior of Al6061-T6 aluminum alloy through tensile testing at various temperatures (T = 25 °C, T = 100 °C, T = 200 °C, and T = 300 °C) using three distinct forecasting methods: Binary Search Tree (BST), Neural Network (NN), and Gaussian Process Regression (GPR). At T = 25 °C, BST exhibits decent accuracy with a low RMSE of 0.6307 and a MAE of 0.4811. However, NN and GPR outperform BST with significantly lower RMSE and MAE values (0.2863 and 0.2266, respectively) and higher R-squared (R^2) values of 0.9997, indicating strong predictive capabilities. Moreover, all methods maintain low Mean Absolute Percentage Error (MAPE) values, confirming their precision. As the temperature rises to T = 100 °C, BST's performance improves but lags behind NN and GPR. At this point, NN and GPR continue to showcase high accuracy with low RMSE and MAE values, along with substantial R^2 values. However, the challenges intensify at T = 200 °C, where BST struggles significantly, revealing a high RMSE and MAE and a lower R^2 value. In contrast, NN and GPR maintain their accuracy, although R^2 values slightly decrease. All methods, nonetheless, demonstrate increased MAPE values, reflecting the complexity of forecasting at high temperatures. Finally, at T = 300 °C, BST's limitations become evident with high

Table 3 Evaluation metrics of forecasting using test data

	RMSE	MAE	R^2	MAPE
T = 25 °C				
BST	0.6307	0.4811	0.9986	0.1320
NN	0.2863	0.2266	0.9997	0.0636
GPR	0.2863	0.2266	0.9997	0.0636
T = 100 °C				
BST	0.5487	0.3808	0.9992	0.1195
NN	0.4624	0.2869	0.9995	0.0924
GPR	0.4624	0.2869	0.9995	0.0924
T = 200 °C				
BST	13.8453	8.8499	0.7045	3.7795
NN	0.6926	0.3466	0.9993	0.1630
GPR	12.7425	8.4275	0.7497	3.6291
T = 300 °C				
BST	6.2365	4.9929	0.8936	3.4890
NN	1.4385	0.5014	0.9943	0.5313
GPR	1.3544	0.3246	0.9950	0.3846

RMSE and MAE values, while NN and GPR sustain their precision. NN stands out with the lowest RMSE and MAE, indicating its superior performance in capturing material behavior under extreme conditions. GPR also performs admirably with low RMSE and MAE values and a high R^2 value. Importantly, both NN and GPR maintain low MAPE values, highlighting their proficiency in delivering accurate forecasts even in challenging scenarios. In summary, the results emphasize that machine learning methods, particularly NN and GPR, excel in accurately predicting the mechanical behavior of Al6061-T6 aluminum alloy, especially under varying and extreme temperatures.

Figure 10 presents the boxplots showing the prediction errors of the BST, NN, and GPR models for Al6061T6 aluminum alloy at temperatures of 25, 100, 200, and 300 °C. The boxplots reveal that the prediction errors of the NN and GPR models are concentrated around zero, indicating their effectiveness in accurately capturing the expected patterns in the strain–stress data across different temperature conditions. In contrast, the prediction errors of the BST model exhibit significant deviations from zero, suggesting challenges in accurately representing the variation in strain–stress data. These boxplots further support the superior performance of the NN and GPR models compared to the BST model in predicting the mechanical behavior of the material.

Based on the results presented, it can be concluded that there is no one approach that consistently outperforms the others in predicting strain–stress curves at different temperature levels. Table 4 provides a comprehensive overview of the performance of each approach. From the computed evaluation scores, it is evident that the NN-based method stands out as the most effective approach for predicting strain–stress curves of the aluminum alloys.

Conclusion

In conclusion, this research aimed to investigate and improve the prediction of stress–strain behavior for the Al6061-T6 as-received material using machine learning methods. The study compared the effectiveness of the bagged trees (BST), neural network (NN), and Gaussian process regression (GPR) models in predicting the mechanical properties of the material at different temperatures.

The results indicated that the NN and GPR models outperformed the BST model in terms of prediction accuracy, as evidenced by lower prediction errors. These models demonstrated their ability to capture the future trends in strain–stress data across various temperature levels. In contrast, the BST model exhibited limitations in accurately capturing the variation in strain–stress data.

Based on the evaluation scores computed, the NN-based method emerged as the most effective approach for predicting the stress–strain curves of the Al6061-T6 alloy. It consistently yielded superior performance compared to the other models considered in this study.

The failure analysis of Al 6061 T6 material revealed its ductile nature, as seen in coalesced micro-voids and microscopic dimples on fracture surfaces. Examining the microstructure during interrupted tests identified intermetallic phase particles as key sites for crack initiation. Initiation mechanisms varied with temperature; particle fracture dominated at temperatures up to 200 °C, while interfacial decohesion prevailed at 300 °C. As deformation continued, cracks propagated perpendicularly to the rolling direction, coalescing in the RD-ND plane, ultimately causing a macroscopic crack to propagate at an angle from the normal direction, leading to catastrophic failure. This analysis enhances our understanding of the material's failure mechanisms, crucial for enhancing its reliability and performance across diverse applications.

As for future work, it is recommended to explore other machine learning-driven prediction methods such as artificial neural networks (ANN) and investigate the applicability of Gaussian process regression for predicting the material behavior of different metal alloys in their as-received form and when subjected to various welding techniques. Additionally, evaluating the performance of BST, NN, and GPR models for predicting material behavior under different temperatures and strain rates is essential. Incorporating deep learning models, known for

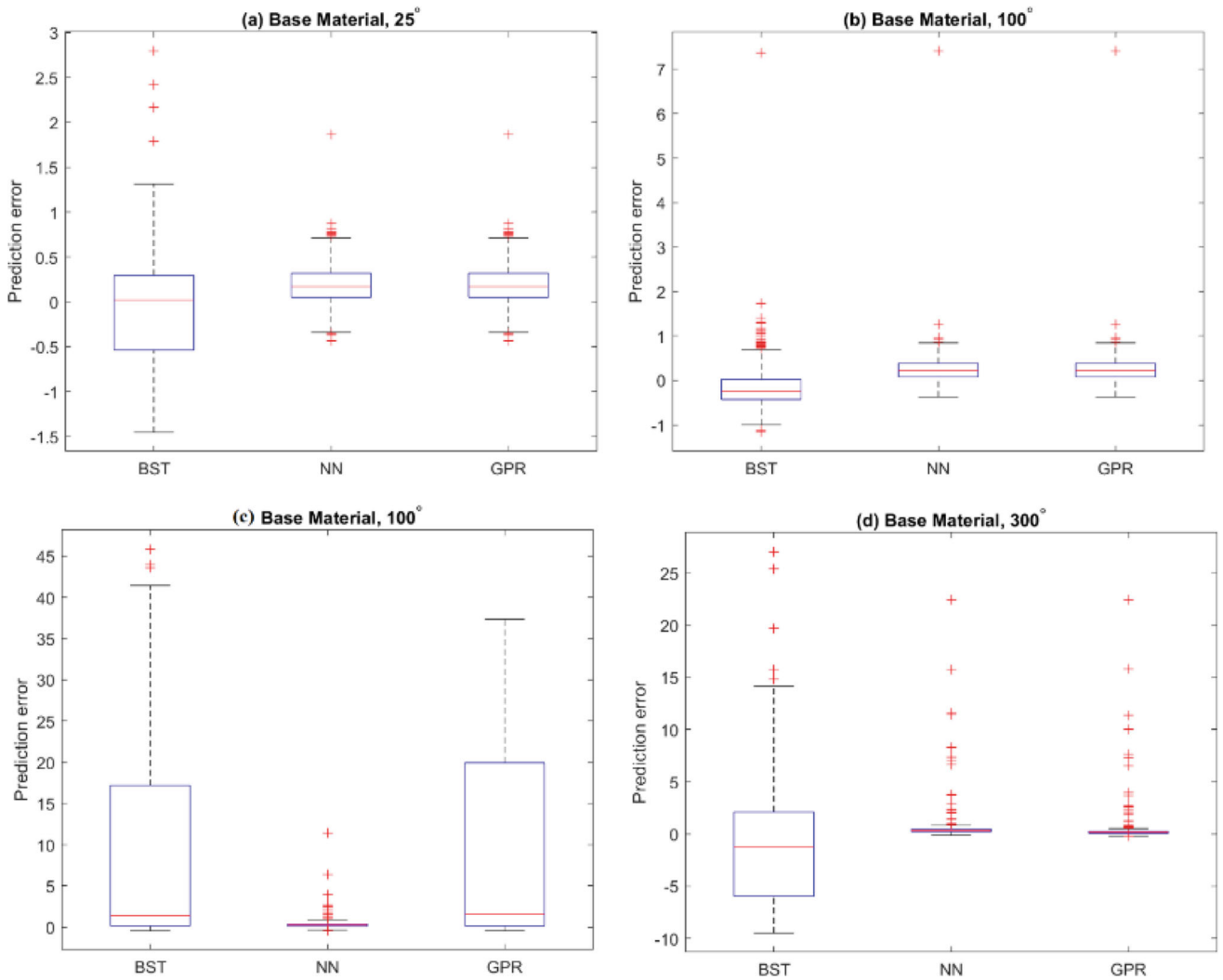

Fig. 10 Distribution of prediction errors using BST, NN and GPR models based on testing data under 25, 100, 200 and 300 °C

Table 4 Averaged performance of the three machine learning methods

Methods	RMSE	MAE	R^2	MAPE
BST	5.315	3.676	0.899	1.880
NN	0.720	0.340	0.998	0.213
GPR	3.711	2.316	0.936	1.042

efficient time-series data modeling, should also be considered in future research endeavors.

References

1. G.A. Edwards, K. Stiller, G.L. Dunlop, APFIM investigation of fine-scale precipitation in aluminium alloy 6061. Appl. Surf. Sci. **76–77**, 219–225 (1994). https://doi.org/10.1016/0169-4332(94)90346-8
2. R.E. Sanders, R. Sanders Jr., Technology innovation in aluminum products. JOM. **53**, 21–25 (2001). https://doi.org/10.1007/s11837-001-0115-7
3. H. Agarwal, A.M. Gokhale, S. Graham, M.F. Horstemeyer, Void growth in 6061-aluminum alloy under triaxial stress state. Mater. Sci. Eng. A. **341**, 35–42 (2003). https://doi.org/10.1016/s0921-5093(02)00073-4
4. Liu N, Ma L, Liu AJ, Zhang Z, Chen MH, Wu YC (2020) Effect of heat treatment on microstructure and mechanical properties of 6061 aluminum alloy containing Sc. Cailiao Rechuli Xuebao Transactions Mater Heat Treat. https://doi.org/10.13289/j.issn.1009-6264.2020-0072
5. Cai J (2016) Effect of heat treatment on microstructure and mechanical properties of 6061 aluminium alloy. Tezhong Zhuzao Ji Youse Hejin/Special Cast Nonferrous Alloy. https://doi.org/10.15980/j.tzzz.2016.09.027
6. Liu W, Wu Y, Deng B, Liu A, Liu W, Xu Z, Ye T (2020) Mechanical properties and microstructure of extruded 6061 aluminum alloy. Jinshu Rechuli/Heat Treat Met. https://doi.org/10.13251/j.issn.0254-6051.2020.09.032
7. M. Nakai, G. Itoh, The effect of microstructure on mechanical properties of forged 6061 aluminum alloy. Mater. Trans. (2014). https://doi.org/10.2320/matertrans.MA201324

8. Alhamidi AA, Dewi M (2018) MICROSTRUCTURAL AND MECHANICAL PROPERTIES AL 6061 PROCESSED BY COLD ROLLING AND AGING. VANOS J Mech Eng Educ. https://doi.org/10.30870/vanos.v3i1.3686
9. Puspasari V, P. A. ING, Mabruri E, Herbirowo S, Utomo EP (2021) THE EFFECT OF ECAP PROCESSING TO HARDNESS, SURFACE MORPHOLOGI, AND CORROSION RESISTANCE OF 6061 ALUMINIUM ALLOYS. Metalurgi. https://doi.org/10.14203/metalurgi.v36i2.589
10. Y. Rong, Y. Huang, L. Wang, Evolution mechanism of transient strain and residual stress distribution in al 6061 laser welding. Crystals. (2021). https://doi.org/10.3390/cryst11020205
11. Y. Huang, X. Meng, Y. Zhang, J. Cao, J. Feng, Micro friction stir welding of ultra-thin Al-6061 sheets. J. Mater. Process. Technol. (2017). https://doi.org/10.1016/j.jmatprotec.2017.07.031
12. A. Dorbane, G. Ayoub, B. Mansoor, R.F. Hamade, A. Imad, Effect of temperature on microstructure and fracture mechanisms in friction stir welded Al6061 joints. J. Mater. Eng. Perform. **26**, 2542–2554 (2017)
13. T. Babu Rao, Stochastic tensile failure analysis on dissimilar AA6061-T6 with AA7075-T6 friction stir welded joints and predictive modeling. J. Fail. Anal. Prev. **20**, 1333–1350 (2020). https://doi.org/10.1007/s11668-020-00937-3
14. D. Thomas, Using artificial intelligence and machine learning for rapidly identifying manufacturing failures. J. Fail. Anal. Prev. **22**, 1813–1815 (2022). https://doi.org/10.1007/s11668-022-01484-9
15. M.S. Babu, T.B. Rao, Development of an in-process cutting tool life prediction system using bidirectional long short-term memory network. J. Fail. Anal. Prev. **23**, 837–845 (2023). https://doi.org/10.1007/s11668-023-01625-8
16. S. Makhfi, A. Dorbane, F. Harrou, Y. Sun, Prediction of cutting forces in hard turning process using machine learning methods: a case study. J. Mater. Eng. Perform. (2023). https://doi.org/10.1007/s11665-023-08555-4
17. Dorbane A, Harrou F, Sun Y (2022) Forecasting FSW material's behavior using an artificial intelligence-driven approach. In: 2022 International Conference on Decision Aid Sciences and Applications (DASA). pp 1553–1557
18. Dorbane A, Harrou F, Sun Y (2022) A tree-driven ensemble learning approach to predict FS welded Al-6061-T6 material behavior. In: 2022 7th International Conference on Frontiers of Signal Processing (ICFSP). IEEE, pp 184–188
19. H.V. Özkavak, M. Ince, E.E. Bıçaklı, Prediction of mechanical properties of the 2024 aluminum alloy by using machine learning methods. Arab. J. Sci. Eng. **48**, 2841–2850 (2022)
20. Y. Hangai, K. Okada, Y. Tanaka, T. Matsuura, K. Amagai, R. Suzuki, N. Nakazawa, Classification of mechanical properties of aluminum foam by machine learning. Mater. Trans. **63**, 257–260 (2022). https://doi.org/10.2320/matertrans.MT-M2021130
21. Devi MA, Prakash CPS, Chinnannavar RP, Joshi VP, Palada RS, Dixit R (2020) An informatic approach to predict the mechanical properties of aluminum alloys using machine learning techniques. In: 2020 International Conference on Smart Electronics and Communication (ICOSEC). pp 536–541
22. X. Cao, Y. Zhang, H. Chen, Predicting mechanical properties and corrosion resistance of heat-treated 7N01 aluminum alloy by machine learning methods. IOP Conf Ser Mater Sci Eng. **774**, 12030 (2020). https://doi.org/10.1088/1757-899X/774/1/012030
23. X. Ye, Z. Su, M. Dahari, Y. Su, S.H. Alsulami, M.S. Aldhabani, A.M. Abed, H.E. Ali, S.M. Bouzgarrou, Hybrid modeling of mechanical properties and hardness of aluminum alloy 5083 and C100 Copper with various machine learning algorithms in friction stir welding. Structures. **55**, 1250–1261 (2023). https://doi.org/10.1016/j.istruc.2023.06.094
24. Z. Xiong, J. Li, P. Zhao, Y. Li, Prediction of mechanical properties of aluminium alloy strip using the extreme learning machine model optimized by the gray wolf algorithm. Adv. Mater. Sci. Eng. **2023**, 5952072 (2023). https://doi.org/10.1155/2023/5952072
25. J. Li, Y. Zhang, X. Cao, Q. Zeng, Y. Zhuang, X. Qian, H. Chen, Accelerated discovery of high-strength aluminum alloys by machine learning. Commun Mater. **1**, 73 (2020). https://doi.org/10.1038/s43246-020-00074-2
26. N. Altinkok, Use of artificial neural network for prediction of mechanical properties of α-Al2O3 particulate-reinforced Al–Si10Mg alloy composites prepared by using stir casting process. J. Compos. Mater. **40**, 779–796 (2005). https://doi.org/10.1177/0021998305055547
27. R. Soundararajan, A. Ramesh, S. Sivasankaran, A. Sathishkumar, Modeling and analysis of mechanical properties of aluminium alloy (A413) processed through squeeze casting route using artificial neural network model and statistical technique. Adv. Mater. Sci. Eng. **2015**, 714762 (2015). https://doi.org/10.1155/2015/714762
28. T. Varol, A. Canakci, S. Ozsahin, Artificial neural network modeling to effect of reinforcement properties on the physical and mechanical properties of Al2024-B4C composites produced by powder metallurgy. Compos. Part B Eng. (2013). https://doi.org/10.1016/j.compositesb.2013.05.015
29. Morinaga M (2019) 6-Aluminum alloys and magnesium alloys. In: Morinaga MBT-AQA to AD (ed) Materials Today. Elsevier, pp 95–130
30. ASTM-B308/B308M-10 (2010) Standard specification for aluminum-alloy 6061-T6 standard structural profile, ASTM International, West Conshohocken, PA, 2010, www.astm.org
31. Materials AS for T and (2011) ASTM E2448-11: standard test method for determining the superplastic properties of metallic sheet materials. American Society for Testing and Materials
32. Y. Xie, K. Zhao, Y. Sun, D. Chen, Gaussian processes for short-term traffic volume forecasting. Transp. Res. Rec. **2165**, 69–78 (2010). https://doi.org/10.3141/2165-08
33. Harrou F, Saidi A, Sun Y, Khadraoui S (2021) Monitoring of photovoltaic systems using improved kernel-based learning schemes N3. IEEE J. Photovolt., https://doi.org/10.1109/JPHOTOV.2021.3057169
34. L. Tang, L. Yu, S. Wang, J. Li, S. Wang, A novel hybrid ensemble learning paradigm for nuclear energy consumption forecasting. Appl. Energy. (2012). https://doi.org/10.1016/j.apenergy.2011.12.030
35. B. Khaldi, F. Harrou, S.M. Benslimane, Y. Sun, A data-driven soft sensor for swarm motion speed prediction using ensemble learning methods. IEEE Sens. J. **21**, 19025–19037 (2021). https://doi.org/10.1109/JSEN.2021.3087342
36. A. Alkesaiberi, F. Harrou, Y. Sun, Efficient wind power prediction using machine learning methods: A comparative study. Energies. **15**(7), 2327 (2022). https://doi.org/10.3390/en15072327
37. Y. Alali, F. Harrou, Y. Sun, A proficient approach to forecast COVID-19 spread via optimized dynamic machine learning models. Sci. Rep. (2022). https://doi.org/10.1038/s41598-022-06218-3
38. C.E. Rasmussen, C.K.I. Williams, *Gaussian processes for machine learning*. (The MIT Press, Cambridge, MA, USA, 2006)
39. Agnihotri A, Batra N (2020) Exploring bayesian optimization. Distill. https://doi.org/10.23915/distill.00026
40. Protopapadakis E, Voulodimos A, Doulamis N (2017) An investigation on multi-objective optimization of feedforward neural network topology. In: 2017 8th International Conference on Information, Intelligence, Systems & Applications (IISA). pp 1–6
41. A.D. Bull, Convergence rates of efficient global optimization algorithms. J. Mach. Learn. Res. **12**, 2879–2904 (2011)

42. B. Shahriari, K. Swersky, Z. Wang, R.P. Adams, N. de Freitas, Taking the human out of the loop: A review of bayesian optimization. Proc. IEEE. **104**, 148–175 (2016). https://doi.org/10.1109/JPROC.2015.2494218
43. J. Elith, J.R. Leathwick, T. Hastie, A working guide to boosted regression trees. J. Anim. Ecol. **77**, 802–813 (2008). https://doi.org/10.1111/J.1365-2656.2008.01390.X
44. J.H. Friedman, Stochastic gradient boosting. Comput. Stat. Data Anal. **38**, 367–378 (2002). https://doi.org/10.1016/S0167-9473(01)00065-2
45. J. Lee, W. Wang, F. Harrou, Y. Sun, Reliable solar irradiance prediction using ensemble learning-based models: A comparative study. Energy Convers. Manag. (2020). https://doi.org/10.1016/j.enconman.2020.112582
46. P. Kumar, S.H. Lai, J.K. Wong, N.S. Mohd, M.R. Kamal, H.A. Afan, A.N. Ahmed, M. Sherif, A. Sefelnasr, A. El-Shafie, Review of nitrogen compounds prediction in water bodies using artificial neural networks and other models. Sustainability. **12**(11), 4359 (2020)
47. A. Yafouz, A.N. Ahmed, N. Zaini, A. El-Shafie, Ozone concentration forecasting based on artificial intelligence techniques: A systematic review. Water Air Soil Pollut. **232**, 79 (2021). https://doi.org/10.1007/s11270-021-04989-5
48. W.C. Lin, C.F. Tsai, Missing value imputation: a review and analysis of the literature (2006–2017). Artif. Intell. Rev. **53**, 1487–1509 (2020). https://doi.org/10.1007/s10462-019-09709-4
49. X. Tang, D. Li, V. Prakash, J.J. Lewandowski, Effects of microstructure on high strain rate deformation and flow behaviour of Al–Mg–Si alloy (AA 6061) under uniaxial compression and combined compression and shear loading. Mater. Sci. Technol. **27**, 13–20 (2011). https://doi.org/10.1179/174328409x428882
50. A. Ghahremaninezhad, K. Ravi-Chandar, Ductile failure behavior of polycrystalline Al 6061–T6. Int. J. Fract. **174**, 177–202 (2012). https://doi.org/10.1007/s10704-012-9689-z
51. H. Bethge, J. Heydenreich, *Electron microscopy in solid state physics*. (Elsevier, 1987)
52. A. Dorbane, G. Ayoub, B. Mansoor, R. Hamade, G. Kridli, A. Imad, Observations of the mechanical response and evolution of damage of AA 6061–T6 under different strain rates and temperatures. Mater. Sci. Eng. A. **624**, 239–249 (2015). https://doi.org/10.1016/j.msea.2014.11.074
53. R.D. Thomson, J.W. Hancock, Ductile failure by void nucleation, growth and coalescence. Int. J. Fract. **26**, 99–112 (1984). https://doi.org/10.1007/bf01157547
54. D. Zhu, B. Mobasher, S.D. Rajan, P. Peralta, Characterization of dynamic tensile testing using aluminum alloy 6061–T6 at intermediate strain rates. J. Eng. Mech. **137**, 669–679 (2011). https://doi.org/10.1061/(asce)em.1943-7889.0000264